ACS APPLIED MATERIALS & INTERFACES
Research Article
www.acsami.org

Energy-Transfer Efficiency in Eu-Doped ZnO Thin Films: The Effects of Oxidative Annealing on the Dynamics and the Intermediate Defect States

Samah M. Ahmed,[†] Paul Szymanski,[‡] Lotfia M. El-Nadi,*[,†] and Mostafa A. El-Sayed*[,‡]

[†]National Institute of Laser Enhanced Sciences, Cairo University, Gamaa St. 1, P.O. Box 11316, Cairo, Egypt

[‡]Laser Dynamics Laboratory, School of Chemistry and Biochemistry, Georgia Institute of Technology, 770 State Street NW, Atlanta, Georgia 30332, United States

Supporting Information

ABSTRACT: We have studied ultrafast dynamics in thin films of Eu-doped zinc oxide (ZnO), prepared by radio-frequency sputtering onto sapphire substrates. Following UV excitation of ZnO, a red emission is observed. Postdeposition annealing in an oxygen atmosphere improves the crystallinity and emission intensity of the films, which are highly sensitive to the dopant concentration. Transient-absorption spectroscopy shows that the excited semiconductor host transfers energy to rare-earth ions on a time scale of only a few picoseconds. The dynamics as a function of the probe wavelength change dramatically after annealing, with annealed films showing the fastest dynamics at much lower wavelengths. Our results show that annealing greatly affects the defect energy levels of the films and the dynamics of the trapped carriers. Unannealed films show dynamics consistent with energy transfer from O vacancies to the dopant, while energy transfer in annealed samples involves acceptor-type defects such as Zn vacancies as intermediates.

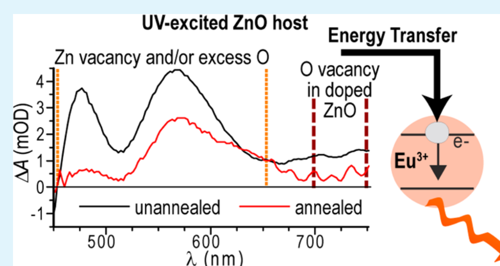

KEYWORDS: *dynamics, emission, energy transfer, europium, transient absorption, zinc oxide*

1. INTRODUCTION

Rare-earth-doped wide-band-gap semiconductors are an interesting class of inorganic luminescent materials with complex optical properties. The complexity is partly due to the carrier dynamics of the host semiconductor. Conventional zinc oxide (ZnO), for example, excited above its band gap of 3.2−3.4 eV has multiple relaxation pathways.[1−5] Exciton recombination between a hole in the valence band (VB) and an electron in the conduction band (CB) produces UV emission. Radiative relaxation where the electron and/or hole occupy trap states within the band gap produces a broad band of blue-green defect emission.[2−5] Finally, nonradiative relaxation may also occur. To optimize the luminescence efficiency and spectrum for applications such as displays and sensors utilizing UV-to-visible downconversion, doping ZnO and other metal oxides with rare earths is an established strategy.[2−4,6] Doping with europium(III) cations (Eu^{3+}), for example, gives rise to an additional narrow red emission band due to the $^5D_0{-}^7F_2$ transition in Eu^{3+}. Of interest is the fact that Eu^{3+} emission is seen upon UV excitation of the ZnO host.[2−4] Thus, the dopant is excited indirectly by energy transfer (ET) from ZnO to Eu^{3+}.

The ET mechanism has been the subject of extensive study.[4] Given that the radiative lifetime of Eu^{3+} is 3 or more orders of magnitude longer than the ZnO exciton lifetime, ET involving an electron in the ZnO CB is extremely unlikely.[1,2,7,8] It has been shown that indirect excitation of Eu^{3+} occurs through a defect level of ZnO.[2,4] The rare-earth emission intensity from Eu-doped ZnO nanowires decreased markedly after annealing in O_2, accompanied by a decrease in the defect emission and fewer O vacancies in the material.[4] This is further evidence that ET occurs through defect levels and that O vacancies in ZnO may create the necessary energy levels.

The challenges to developing these materials for many commercial applications include fabrication on different substrate types with good crystallinity and control of the level of doping, so that the electrical and optical properties are both optimized. Radio-frequency (RF) sputtering is an established and commercially viable method for producing thin films of materials such as nitrides and oxides.[9−11] We have applied this method to form amorphous, oxygen-rich ZnO films with varying levels of Eu dopant that can be annealed into polycrystalline films. By growing films on transparent sapphire substrates, we could perform time-resolved absorption measurements in transmission mode as a function of the Eu concentration and compare the results to steady-state photoluminescence (PL) measurements on the same samples. The most efficient ET occurs with a time constant of 1−4 ps independent of the sample conditions, but the defects that couple most efficiently to Eu are different for annealed and

Received: October 28, 2013
Accepted: January 3, 2014
Published: January 3, 2014

 © 2014 American Chemical Society dx.doi.org/10.1021/am404662k | ACS Appl. Mater. Interfaces 2014, 6, 1765−1772

Table 1. Parameters for the (002) Peaks of ZnO Thin Films, Both As-Deposited at Room Temperature ("RT") and Annealed at 600 °C after Deposition

	2θ (deg)		c (Å)		fwhm (deg)		average grain size (nm)	
sample	RT	600 °C	RT	600 °C	RT	600 °C	RT	600 °C
ZnO	34.28	34.42	5.228	5.206	0.23	0.20	36	41
1Eu	33.82	34.42	5.297	5.207	0.37	0.30	23	26
3Eu	33.63	34.39	5.326	5.211	0.94	0.33	9	24
5Eu	33.63	34.34	5.326	5.218	0.87	0.49	10	17

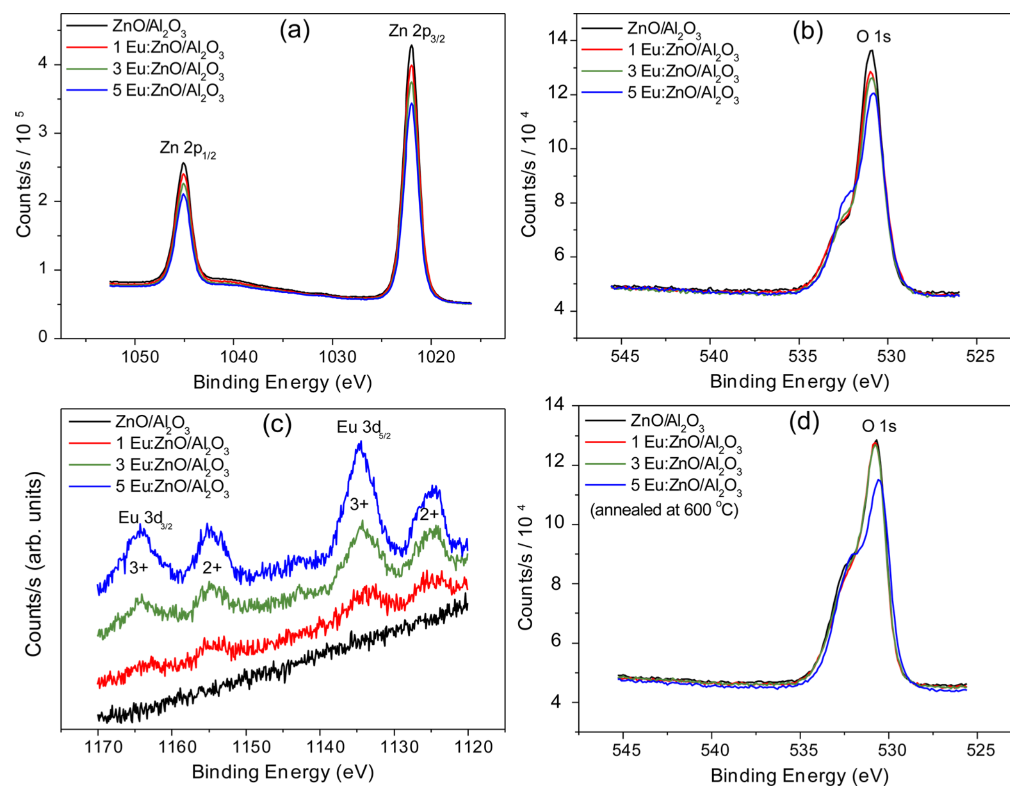

Figure 1. XPS spectra for as-sputtered films in the (a) Zn, (b) O, and (c) Eu regions. (d) Oxygen XPS spectra of the series of films after annealing.

unannealed samples. Our results show that ultrafast ET can occur in ZnO without significant O vacancies and may involve other states such as Zn vacancies.

2. EXPERIMENTAL SECTION

2. 1. Thin-Film Deposition and Characterization. Eu-doped ZnO sintered pellets, with different molar concentrations of Eu_2O_3 (0, 1, 3, and 5 mol %), were prepared to be used as targets in RF sputtering deposition. Calculated amounts of ZnO and Eu_2O_3 powders were thoroughly mixed in an agate mortar for good homogeneity and then cold-pressed under 5000 kg/cm^2 into pellets of diameter of ~3.18 cm. Finally, the pellets were sintered in a furnace (Lindberg Blue M) in ambient air at a temperature of 1100 °C for 6 h with a heating rate of 10 °C/min. After sintering, the pellets became more compact and ceramic-like, and their diameter decreased to ~2.7 cm (thickness of ~1.25 mm). Furthermore, the color of the sintered undoped ZnO pellet changed to light yellow, while all Eu-doped ZnO pellets kept the white color.

The substrates used in the present study are single-crystal *c*-plane sapphire substrates from MTI Corp., 12 × 12 mm with a thickness of 0.5 mm. Prior to deposition, all substrates were cleaned ultrasonically for 5 min in acetone, isopropyl alcohol, ethanol, finally deionized water, and then dried by N_2 gas. Thin films were deposited at room temperature by RF sputtering (Kurt Lesker PVD75) with a power of 100 W and in an atmosphere of argon gas at a pressure of 5 mTorr while rotating the substrates at ~2 rpm. The deposition time was 65 min. A commercial ZnO (99.99%) target was used for deposition of undoped ZnO thin films. For Eu-doped thin-film deposition, two Eu-doped ZnO sintered pellets were placed on the commercial ZnO target. The prepared thin films were labeled according to the Eu_2O_3 mol % of the target pellets. The prepared thin films were smooth and mirror-like to the naked eye. After deposition, half of the prepared thin films were annealed in a horizontal tube furnace (Lindberg Blue M) at a temperature of 600 °C for 30 min, under a continuous flow of oxygen gas and with a heating rate of 5 °C/min. After annealing, films were cooled to room temperature in an oxygen atmosphere.

The crystalline phase structures of all thin films were investigated by X-ray diffraction (XRD) using an Alpha-1 X'Pert diffractometer with a Cu Ka radiation source (λ = 1.54056 Å), operating at 45 kV and 40 mA. The XRD patterns of all thin films were recorded in a continuous 2θ range of 17−75°, with 0.02° and 45 s/step. For incident beam optics, a 0.5° divergence slit was used with a 1° antiscatter slit. No solar slit was used. A 10-mm mask was used to fix the beam size according to the sample dimension. For the diffracted beam optics, a 5.5° diffracted beam antiscatter slit was used, and no solar slit was used.

X-ray photoelectron spectroscopy (XPS) measurements of all thin films were carried out using a Thermo K-Alpha instrument under an ultrahigh-vacuum background pressure of ~10^{-8} mbar. During the measurements, the flood gun was enabled in order to compensate for the charge accumulation on the sample surface. Furthermore, the derived binding energies were calibrated by setting the measured

Table 2. Atomic Fractions in the Thin Films, Both As-Deposited at Room Temperature ("RT") and Annealed at 600 °C after Deposition

sample	% O		% Zn		% Eu		O:Zn	
	RT	600 °C	RT	600 °C	RT	600 °C	RT	600 °C
ZnO	50.50	57.41	49.50	42.59	0	0	1.020	1.348
1Eu	51.87	57.42	47.68	41.95	0.45	0.63	1.088	1.369
3Eu	53.40	59.09	45.60	39.52	1.00	1.39	1.171	1.495
5Eu	55.47	63.03	42.45	34.35	2.08	2.62	1.307	1.835

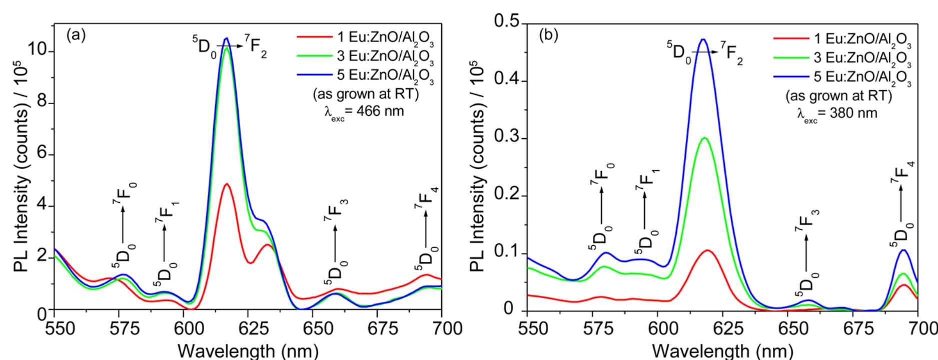

Figure 2. PL spectra of Eu-doped ZnO thin films on sapphire substrates as grown at room temperature ("RT") without annealing, measured at excitation wavelengths of (a) 466 nm and (b) 380 nm. The same integration time was used to measure all PL intensities.

binding energy of the C 1s peak to 284.6 eV.[12,13] The analyzed area was shown to be 400 × 400 μm. The data analysis was done by *Avantage* software.

2. 2. PL. The PL measurements of all thin films were carried out at room temperature using a spectrofluorometer (Fluorolog 3, Horiba Scientific). The optical excitation source was a 450 W xenon lamp, equipped with a single-grating monochromator as well as a photodiode for excitation correction. A variable-angle sample holder was used to mount the thin films at an angle of 60° from the excitation slit. Emission was dispersed by a monochromator (IHR 320) and then detected by a photomultiplier tube (R928P) in the photon-counting mode. Spectra were acquired with a step size of 1 nm and an integration time of 3 s/step.

2. 3. Ultrafast Transient Absorption (TA). TA dynamics measurements were carried out with a Helios UV−visible spectrometer (Ultrafast Systems) with a time range of ~3 ns. The pump light was at 380 nm, obtained from the fourth harmonic of the signal from a Coherent OPerA Solo optical parametric amplifier, which was pumped by a Coherent Libra regeneratively amplified Ti:sapphire laser (809 nm, 50 fs pulses, 1 kHz repetition rate). The broad-band probe beam was produced by focusing a small fraction of the fundamental wavelength into a sapphire crystal. Both the pump and probe were focused and overlapped on the surface of the thin film. The energy incident on the sample was 240 nJ/pulse. A long-pass filter (cut wavelength at 420 nm) was used to prevent scattered pump light from reaching the detector, which can cause spectral artifacts including a negative peak at 760 nm due to second-order diffraction of the pump light from the spectrometer grating. Data were analyzed in *Matlab* (Mathworks) software using the Nedler−Mead simplex algorithm for fitting and Monte Carlo with 1000 simulated data sets for uncertainty estimates.

3. RESULTS AND DISCUSSION

3. 1. XRD and Photoemission. The XRD patterns of each thin film contained only the (006) peak due to the *c*-plane single-crystal sapphire substrate and the (002) and (004) peaks of wurtzite ZnO.[14] Signals corresponding to Eu_2O_3 were not observed. As-sputtered at room temperature, the films are highly textured and have a preferred orientation along the *c* axis perpendicular to the substrate.[15−17] The lattice parameter *c* was calculated from the Bragg angle of the ZnO (002) diffraction peak.[17,18] Scherrer's equation was used to estimate the average grain size.[17] The results are given in Table 1, with the (002) peaks shown in Figure S1 (in the Supporting Information, SI).

In the as-sputtered films, Eu doping enlarged the unit cell and degraded the crystal quality of wurtzite ZnO. This is expected if Zn^{2+} ions (0.74 Å atomic radius) are substituted by Eu^{3+} ions (1.07 Å atomic radius), consistent with the literature results.[15,16,19,20] Annealing improves the crystallinity of each film, although the most heavily doped films are still slightly distorted with smaller average grain sizes compared to pure ZnO.

With XPS, the presence of Zn^{2+} was confirmed by the characteristic peaks at 1045 and 1022 eV (Figure 1).[13] In the doped films, Eu is present as both Eu^{3+} and Eu^{2+},[20,21] with the atomic fraction of Eu increasing with increasing amounts of Eu in the precursor materials. Annealing causes little change to the Zn or Eu peaks. The O^{2-} peak is accompanied by a higher-energy shoulder, whose intensity increases after annealing (not shown). This shoulder has been attributed to both defects[22,23] and chemisorbed oxygen.[24] Analysis of the XPS data gives the atomic fraction of each element (Table 2). The O content increases with the amount of Eu in the film, even before annealing, suggesting that some of the O may exist in Eu_2O_3 domains. Because O:Zn ratios as high as 1.835 are not realistic for bulk ZnO, significant amounts of O and/or Eu_2O_3 must be present at the surface.

3. 2. PL. Figure 2 shows the PL for unannealed samples at excitation wavelengths of 466 nm (a), which is absorbed only by Eu^{3+} ions (the $^7F_0 \rightarrow {}^5D_2$ transition), and 380 nm (b), which is not absorbed by Eu^{3+}. Ellipsometry measurements give a band gap of 3.25 eV for the undoped sputtered films (Table S1 in the SI), so the absorption at 380 nm is the band-edge absorption of ZnO. When Eu^{3+} is excited directly (Figure 2a), the characteristic emission lines of Eu^{3+} are seen. Rare-earth emission was also observed after absorption of UV light by ZnO (Figure 2b). In fact, the two excitation wavelengths

dx.doi.org/10.1021/am404662k | ACS Appl. Mater. Interfaces 2014, 6, 1765−1772

produce similar spectra except UV excitation yields significantly lower emission intensity. The contribution from ZnO defect emission in Figure 2b is weak at best. This indirect excitation of Eu has been reported previously and ascribed to ET from ZnO to Eu.[2−4] No ZnO excitonic emission below 400 nm is observed, even when higher-energy photons are used for excitation.

Similar behavior is observed in annealed samples (Figure 3), although Eu^{3+} emission following UV absorption by ZnO is significantly more intense. Traces of ZnO emissions are seen at an excitation wavelength of 340 nm, at the expense of lower Eu^{3+} emission. Indirect excitation is most efficient at 380 nm, where ZnO emission is not observed. In fact, at lower concentrations of Eu, excitation at 380 nm produces more emission than direct excitation of Eu^{3+}. Therefore, at 380 nm ET from radiative sites in ZnO to Eu^{3+} is nearly 100% efficient, although not all Eu^{3+} ions will necessarily produce emission.

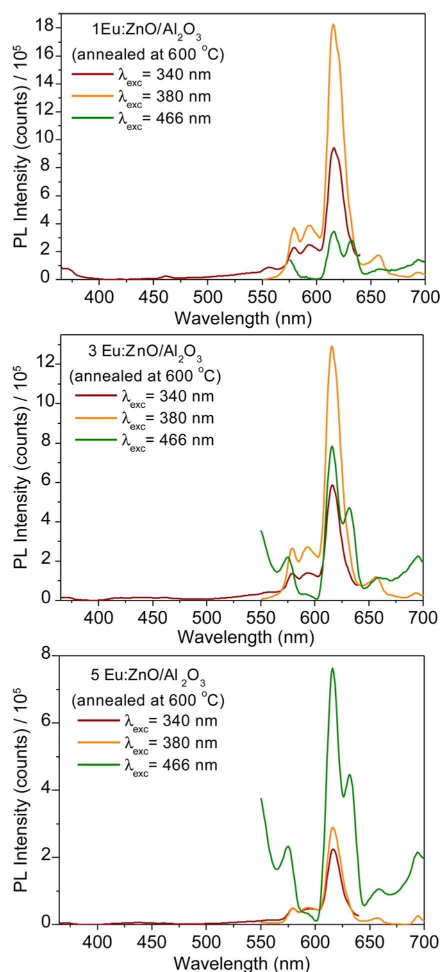

Figure 3. PL spectra of Eu-doped ZnO thin films on sapphire substrates after annealing at 600 °C, measured at different excitation wavelengths. The same integration time was used to measure all PL intensities. Indirect excitation of Eu through ET from ZnO is most efficient at the 380 nm band edge. In samples 1Eu:ZnO and 3Eu:ZnO, indirect excitation is also more efficient than direct excitation of Eu.

Figure 4 compares the Eu^{3+} emission intensity as a function of the composition and annealing for indirect and direct excitation. For both unannealed and annealed films, emission due to direct excitation increases from 1Eu to 3Eu but then saturates. The saturation can be explained by concentration quenching, nonradiative relaxation due to Coulombic interactions between ions, as has been observed in other rare-earth-doped semiconductors.[25−27]

For indirect excitation at 380 nm, the rare-earth emission increases monotonically with the dopant concentration for unannealed films (Figure 4a). Annealing increases the emission intensity by 1 order of magnitude, but the trend is reversed and the maximum intensity occurs for the least-doped sample. The concentration dependence can be explained if there are multiple types of Eu sites within the films, some of which are inactive or inefficient for ET and emission under the UV-excitation pathway. Because Eu occupies Zn sites,[15,16,19,20] the properties of the dopant should be heavily influenced by the nature of the surrounding O sites. The distribution of sites changes with annealing in the presence of O_2, as supported by O enrichment of the films after annealing (Table 2).

3. 3. TA. To further understand the differences in Eu^{3+} emission from the series of thin films, we carried out femtosecond dynamics measurements. The excitation wavelength was tuned to 380 nm, which gives the maximum emission intensity for indirect excitation (Figure 3). Over the probe region of 450−900 nm, the TA spectra at zero delay are broad and complex with multiple overlapping features (Figure 5). The induced absorption ($\Delta A > 0$) is likely a combination of trapped electrons and holes, as has been reported in ZnO[28] and TiO_2,[29−31] because these wavelengths are within the band gap. For the unannealed films, the spectra of all of the samples are similar except for increasing absorption over the 700−800 nm region as the Eu concentration increases.

Compared with TA spectra of ZnO colloids[28] and spectroelectrochemical data on ZnO thin films in an electrolyte solution,[32] our TA spectra contain additional features below ~650 nm. The lifetime of the signal in each region of the spectrum is generally similar (Figure S2 in the SI). Annealing at 600 °C led to a marked decrease in induced absorption from 450−750 nm, which includes the region in question. Thus, the additional induced absorption is caused by physical and/or chemical features associated with poorer crystal quality, i.e., defect states and possibly impurities such as chemisorbed carbon.

Representative dynamics data for undoped and doped (5Eu) samples, integrated over wavelengths of 700−750 nm are shown in Figure 6. The rise times are significantly less than 1 ps, comparable to the instrument response. The signal from pure ZnO is dominated by a decay over a time scale of hundreds of picoseconds due to charge-carrier trapping and recombination, in agreement with other studies.[1,7,28,32,33] The decay traces for doped and undoped samples in the same set of films (annealed or unannealed) are similar for delay times over ~300 ps, with comparable decay rates but possibly different amplitudes. Differences caused by doping with Eu are evident at earlier delay times.

Each data set from the doped samples is fit to the sum of an exponential decay, representing the change in dynamics caused by doping with Eu, and a scaled background representing the decay of excitation in undoped ZnO. For the background, the TA signal (integrated over multiple wavelengths) from undoped ZnO is used, multiplied by an adjustable scaling factor:

$$\Delta A_{\text{Eu-ZnO}}(t) = A_{\text{d}} e^{-t/\tau_{\text{d}}} + c\Delta A_{\text{ZnO}}(t) \quad (1)$$

The complex multiexponential dynamics of the thin film over its broad TA spectrum is thus reduced to three parameters.

dx.doi.org/10.1021/am404662k | ACS Appl. Mater. Interfaces 2014, 6, 1765−1772

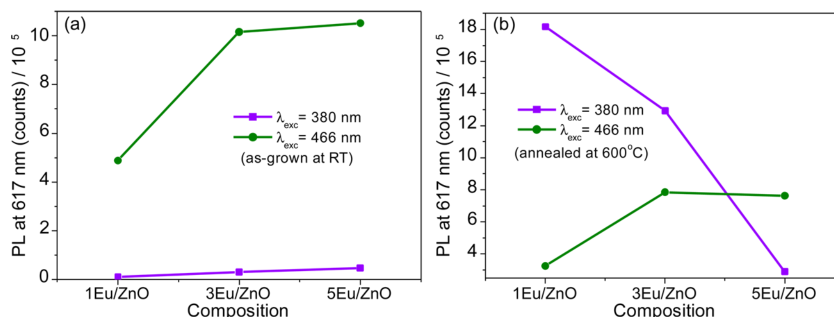

Figure 4. PL intensity of the Eu^{3+} band at 617 nm for (a) thin films deposited at room temperature ("RT") and (b) thin films annealed at 600 °C after deposition. Direct Eu excitation at 466 nm is compared with indirect excitation at 380 nm. The same integration time was used to measure all PL intensities.

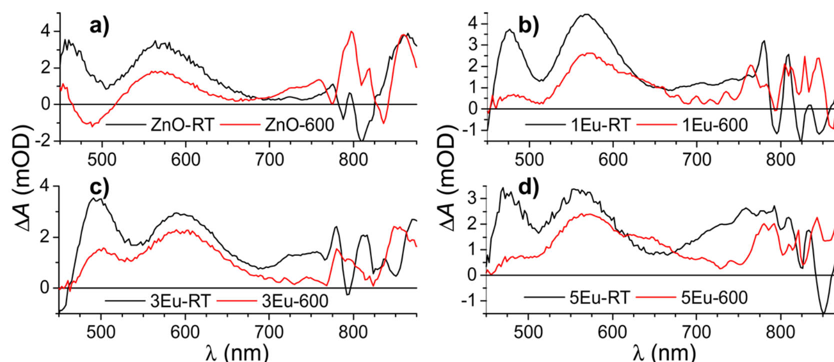

Figure 5. TA spectra at zero pump−probe delay for ZnO thin films, comparing those deposited at room temperature ("RT") with those annealed at 600 °C ("600") after deposition: (a) undoped; (b) doped 1Eu; (c) doped 3Eu; (d) doped 5Eu.

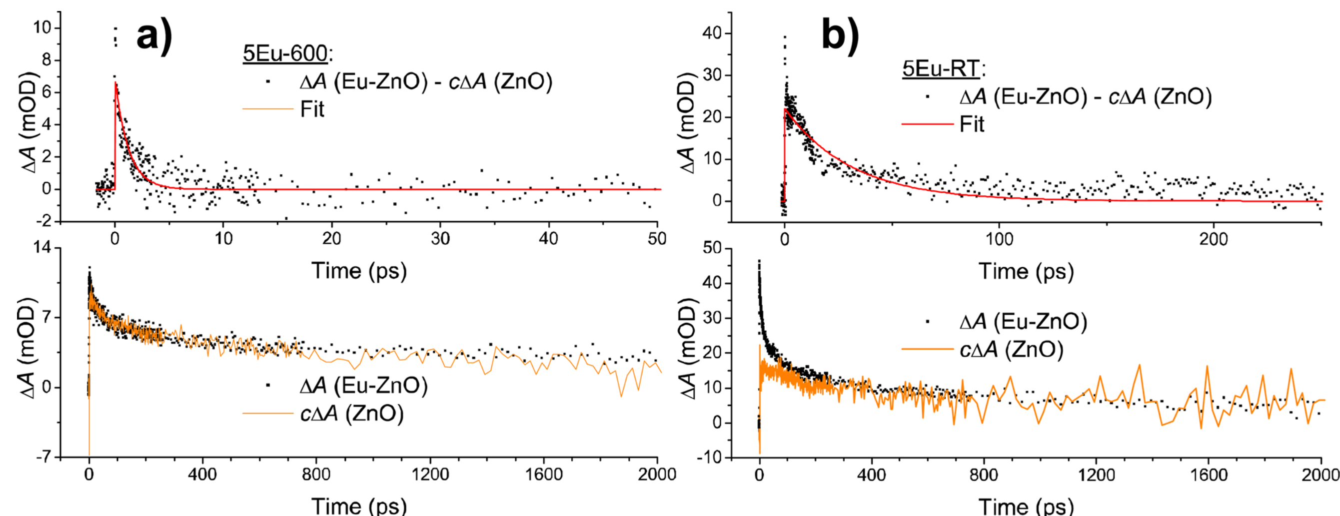

Figure 6. Representative TA dynamics for doped (5Eu) and undoped thin films (a) annealed at 600 °C after deposition and (b) deposited at room temperature ("RT") without annealing. Probe wavelengths of 700−750 nm were integrated. The lower panels give the experimental data, with the ZnO data scaled to best fit the long-delay dynamics of Eu-ZnO. The upper panels show the data with the second term on the right side of eq 1 subtracted, with the fit to the first term on the right side of eq 1. Decay rates are similar for undoped and doped samples except at early delay times, as reflected on the upper panels. The data include a transient spike/artifact near zero delay, which is not accounted for in the fit.

This method is identical with the "subtractive" analysis used to determine the ET time in Eu-doped ZnO nanowires[4] but extended to multiple wavelengths. The scaling factor that is applied to the signal from undoped ZnO takes into account the uncertainty in comparing intensities between measurements in TA because of the great sensitivity of the signal on pump−probe overlap, which may vary over the course of a days-long experiment.

The TA spectra were integrated over a range of wavelengths, subtracting any baseline signal from negative delays (probe before pump) 1 ps or more before time zero. The integration and modeling was carried out on 50-nm segments of the spectrum excluding any wavelengths where signals could be obscured by scattered pump light (despite the presence of the long-pass filter). Results are presented in part in Table 3 and in full in the SI (Table S2). The model was also applied to the

Table 3. Decay Time Constants and Uncertainties over Different Wavelength Regions for Unannealed ("RT") and Annealed ("600 °C") Samples

	τ_d(550−600 nm) (ps)		τ_d(600−650 nm) (ps)		τ_d(650−700 nm) (ps)		τ_d(700−750 nm) (ps)	
sample	RT	600 °C	RT	600 °C	RT	600 °C	RT	600 °C
1Eu	28 ± 4	2.7 ± 0.3	28 ± 3	4.1 ± 0.5	13.5 ± 0.6	7.9 ± 0.7	1.6 ± 0.2	24 ± 5
3Eu	70 ± 10	1.9 ± 0.3	44 ± 9	3.2 ± 0.4	7.9 ± 0.5	12 ± 2	1.0 ± 0.2	23 ± 3
5Eu	80 ± 10	1.3 ± 0.1	50 ± 10	2.1 ± 0.4	7.7 ± 0.7	12 ± 6	1.2 ± 0.3	31 ± 5

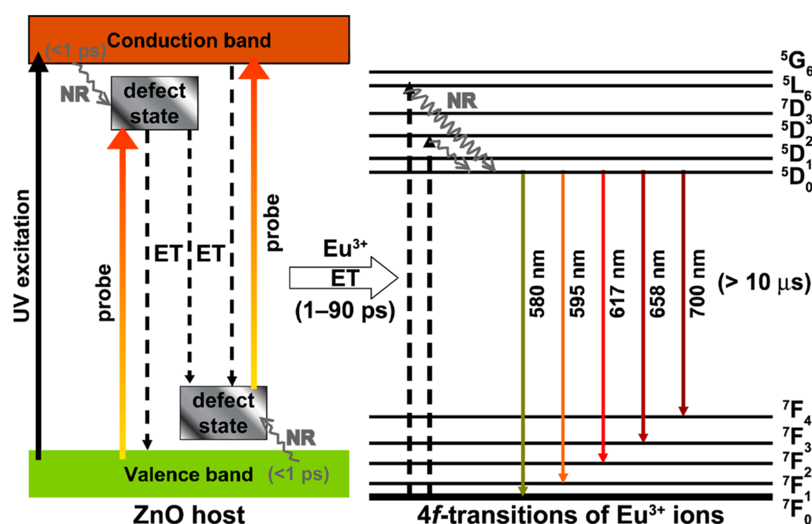

Figure 7. Energy-level diagram illustrating possible pathways involved in pump−probe spectroscopy of ZnO defects, nonradiative relaxation ("NR"), energy transfer ("ET", dashed lines), and Eu^{3+} radiative transitions. Time constants for major processes are shown, with ZnO excitonic and defect-level emission omitted because of quenching due to efficient ET.

500−550, 775−825, and 825−875 nm regions, but satisfactory fits were not obtained.

The model captures the essential features in the data for delay times below 500 ps and is successful at fitting the ultrafast changes in the dynamics caused by the addition of Eu. While τ_d varies significantly with sample annealing and the probe wavelength, it shows a much weaker dependence on the Eu^{3+} concentration; the time constant either is similar for all concentrations or is different for 1Eu samples only.

3. 4. Mechanism Responsible for ET. Analysis of the dynamics reveals that a new decay component with time constant 1−90 ps is added by doping (Table 3), with the value depending on the probe wavelength, dopant concentration, and annealing. These dynamics are at least competitive with, and often faster than, reported radiative lifetimes of ZnO exciton-level emission, which range from ∼20 ps to ∼1 ns.[7,33,34] Defect-level emission decays on the microsecond time scale,[35] significantly slower than τ_d. Thus, Eu can quench ZnO emission consistent with steady-state PL measurements (Figure 3), which show the dominance of Eu^{3+} emission following 380-nm excitation of the ZnO host. Because the Eu^{3+} radiative lifetime is at least 10 μs and cannot be reflected in the TA data,[4] we interpret τ_d to be the time for ET from ZnO to Eu^{3+}.

Figure 7 illustrates the energy levels involved in ET from ZnO to Eu^{3+} and the subsequent emission from rare-earth ions.[2,4] Emission from ZnO excitonic and defect states is quenched in Eu-doped samples (Figure 3) and is not shown. The locations of the defect states that serve as intermediates, which are also responsible for defect-level emission, are depicted as close to the band edges. ET excites a Eu^{3+} ion within the ZnO host, while the electron within the initially unoccupied defect state relaxes back to the VB.[2,4,32,36,37] Alternatively, relaxation of a CB electron to a deep hole trap may lead to emission or ET to Eu^{3+}.[5,38] For example, a complex between two defects (Zn and O vacancies) gives rise to a hole trap ∼0.88 eV above the VB edge, which has been implicated in green defect emission.[39]

The broad induced TA (Figure 5), which exists in both the doped and undoped ZnO, suggests that the femtosecond laser is primarily probing defect states of ZnO, with trapping occurring on a time scale much shorter than 1 ps. This induced absorption could reflect excitation of trapped electrons to the CB, trapped holes to the VB, electrons between defect sites, or a combination of all of these. Femtosecond TA on Eu-doped ZnO was carried out previously by Wang et al. at a single probe wavelength of 700 nm and analyzed by the model (eq 1) shown above.[4] ZnO in this previous study was oxygen-deficient.[4] The change in the induced absorption decay caused by doping with 1.2 atom % Eu was 9 ± 1 ps for unannealed samples compared to 130 ± 4 ps for samples annealed in O_2 at 600 °C.[4] The decay was attributed to ET from ZnO to Eu^{3+}, with the decrease in efficiency caused by annealing explained as a reduction in the number of O vacancies.[4] Thus, ET originates from O vacancies transiently populated after absorption of a photon at the ZnO band edge.

For our thin films probed at 700−750 nm, even faster decay components were measured (Table 3) with a ∼20 times slower decay after annealing in O_2 at 600 °C. O vacancies, neutral or positively charged, may exist in our films because they are not formed in an O-rich environment; however, they should exist in lower numbers after the O enrichment that occurs with annealing (Table 2).[40] Therefore, it seems plausible that O vacancies could play a role in ET in our films as well. Density functional theory predicts that an O vacancy in the

thermodynamically stable 2+ charge state gives rise to an initially unoccupied level 0.3−0.6 eV below the CB minimum,[41−43] although one study states that it is resonant with the CB.[44] The probe photon energy of 1.65−1.77 eV (between 750 and 700 nm) is thus sufficient to excite an electron trapped in this state to the CB. The intensity of the TA signal (Figure 5) from Eu-doped samples decreases significantly in this region after annealing in O_2, accompanied by an increase in the O:Zn ratio (Table 2), further supporting the assignment of the signal to O vacancies.

In both the 550−600 and 600−650 nm regions, the opposite behavior is observed: τ_d decreases by a factor of ∼10−80 after annealing in O_2 at 600 °C (Table 3). The O:Zn ratio (Table 2) and rare-earth emission intensity (Figure 4) under 380 nm excitation both increase significantly upon annealing as well. Finally, the induced absorption (Figure 5) in these regions decreases with annealing but by a smaller fraction, consistent with the presence of significant defects postannealing. We propose that τ_d for states that absorb at these wavelengths also reflects defect-mediated ET, albeit from other types of defects. Defects with the lowest formation energies under O-rich conditions are believed to be Zn vacancies, which are acceptor-type levels.[40,45,46] Zn vacancies or complexes involving Zn vacancies lie 1.7−3.1 eV below the CB minimum (∼0.1−1.5 eV above the VB minimum).[34,39,47] These intermediates are within the probe photon energy for electron transitions to the CB and/or from the VB. Such defects are possibly involved in the green PL from ZnO,[34,35,39,45,48] thus providing energy for the $^7F_0 \rightarrow {}^5D_1$ or $^7F_0 \rightarrow {}^5D_0$ (normally forbidden, but possible at low-symmetry sites) transitions[2] of Eu^{3+}.

O interstitials and O antisite defects are also possible under O-rich conditions but have higher formation energies.[40,45−47] O antisites and interstitials are reported to be 2.4 and 2.3−3.0 eV below the CB minimum, respectively.[34] These defects have been considered for their role in ZnO visible emission,[34] and their energies are relevant to both defect-mediated ET and the TA spectra reported here. Given the broad nature of the TA and PL spectra, there may be a variety of defects present in a given film.

The presence of Eu is always associated with an increased O:Zn ratio (Table 2). Furthermore, the defect states found in annealed samples (Figure 5) are also found in unannealed samples. Thus, the films may contain O-rich domains and surface deposits because of the presence of Eu_2O_3 even before annealing. The dynamics results (Table 3) do show that these domains may give rise to ET even in unannealed films, but they are not the most efficient. The loss of O vacancies and change in crystallinity after annealing should change the defect density of states considerably, which is reflected in the TA spectra (Figure 5), and the dynamics are affected as well.

The effect of Eu doping on the dynamics in the 650−700 nm region (Table 3) does not show a clear trend with either the Eu concentration or annealing. Because this is a lower-intensity region in the TA spectra (Figure 5), absorption at these wavelengths likely represents the tail of one or both of the regions discussed above. There may also be contributions from defects that are inactive in ET.

We next consider the steady-state PL intensity from rare-earth emission (Figure 4). As stated above, the emission with 380 nm excitation can be explained if there are multiple types of defect sites in the film, not all of which are active in ET. All unannealed samples show significant absorption from 700 to 750 nm (Figure 5), which increases monotonically with increasing Eu concentration and decreases substantially after annealing. This absorption is likely from O vacancies promoted by the incorporation of Eu atoms within the ZnO lattice. For annealed samples, the PL intensity decreases with the Eu concentration (Figures 3 and 4) more quickly than the O:Zn ratio increases (Table 2). This shows that there are competing relaxation pathways involving defects, only a minority of which lead to ET. Further supporting this conclusion is the fact that τ_d (Table 3) does not follow the same trend as the PL intensity (Figure 4) with changing the Eu concentration (Table 2). Because of the complexity of the TA spectra (Figure 5), further assigning the multiple overlapping features to ET-active and -inactive defects will require further experiments, which could include annealing in different atmospheres and chemical modification of the thin-film surface.

4. CONCLUSIONS

We have synthesized Eu-doped ZnO thin films by RF sputtering of targets and deposition on sapphire substrates. Efficient UV-to-red converting devices can be produced by a lightly Eu-doped, O-rich material with good crystallinity by conventional film-deposition techniques. X-ray data are consistent with the incorporation of Eu in the ZnO lattice. Annealing at high temperatures in an atmosphere of oxygen caused a 1 order of magnitude increase in rare-earth emission following excitation of the ZnO host at 380 nm. TA measurements show a significant decrease in the defect density along with a change in the wavelength-dependent dynamics. The dynamics point to ultrafast ET from ZnO to Eu^{3+}, which favors different defect states as intermediates for annealed and unannealed films. Our results are consistent with defect-mediated ET involving O vacancies for unannealed samples compared to Zn vacancies and/or excess O atoms for annealed samples.

■ ASSOCIATED CONTENT

Ⓢ Supporting Information

XRD data in the ZnO (002) region, TA spectra at multiple delay times, table of band-gap energies and film thicknesses, and table of dynamics fitting parameters. This material is available free of charge via the Internet at http://pubs.acs.org.

■ AUTHOR INFORMATION

Corresponding Authors

*E-mail: mtprlotfia@gmail.com.

*E-mail: melsayed@gatech.edu.

Notes

The authors declare no competing financial interest.

■ ACKNOWLEDGMENTS

This work was financially supported by the U.S. National Science Foundation (Grant OISE-1103827) and the Department of Egyptian Cultural and Educational Affairs, Ministry of Higher Education (fellowship for S.M.A.). We thank Eric Woods from the Georgia Institute of Technology for performing the ellipsometry measurements and assisting with ellipsometry data analysis.

■ REFERENCES

(1) Cavaleri, J. J.; Skinner, D. E.; Colombo, J. D. P.; Bowman, R. M. *J. Chem. Phys.* **1995**, *103*, 5378−5386.

(2) Peres, M.; Cruz, A.; Pereira, S.; Correia, M. R.; Soares, M. J.; Neves, A.; Carmo, M. C.; Monteiro, T.; Pereira, A. S.; Martins, M. A.; Trindade, T.; Alves, E.; Nobre, S. S.; Sá Ferreira, R. A. *Appl. Phys. A: Mater. Sci. Process.* **2007**, *88*, 129−133.
(3) Mordkovich, V. Z.; Hayashi, H.; Haemori, M.; Fukumura, T.; Kawasaki, M. *Adv. Funct. Mater.* **2003**, *13*, 519−524.
(4) Wang, D.; Xing, G.; Gao, M.; Yang, L.; Yang, J.; Wu, T. *J. Phys. Chem. C* **2011**, *115*, 22729−22735.
(5) Wang, Z.; Lin, C.; Liu, X.; Li, G.; Luo, Y.; Quan, Z.; Xiang, H.; Lin, J. *J. Phys. Chem. B* **2006**, *110*, 9469−9476.
(6) Shen, W. Y.; Pang, M. L.; Lin, J.; Fang, J. *J. Electrochem. Soc.* **2005**, *152*, H25−H28.
(7) Teke, A.; Özgür, Ü.; Doğan, S.; Gu, X.; Morkoç, H.; Nemeth, B.; Nause, J.; Everitt, H. O. *Phys. Rev. B* **2004**, *70*, 195207.
(8) Sun, C.-K.; Sun, S.-Z.; Lin, K.-H.; Zhang, K. Y.-J.; Liu, H.-L.; Liu, S.-C.; Wu, J.-J. *Appl. Phys. Lett.* **2005**, *87*, 023106.
(9) Davidse, P. D. *Vacuum* **1967**, *17*, 139−145.
(10) Ozgur, U.; Alivov, Y. I.; Liu, C.; Teke, A.; Reshchikov, M. A.; Dogan, S.; Avrutin, V.; Cho, S. J.; Morkoc, H. *J. Appl. Phys.* **2005**, *98*, 041301.
(11) Vossen, J. L. *J. Vac. Sci. Technol.* **1971**, *8*, S12−S30.
(12) Li, G.-R.; Dawa, C.-R.; Lu, X.-H.; Yu, X.-L.; Tong, Y.-X. *Langmuir* **2009**, *25*, 2378−2384.
(13) Du, Y.-P.; Zhang, Y.-W.; Sun, L.-D.; Yan, C.-H. *J. Phys. Chem. C* **2008**, *112*, 12234−12241.
(14) Liu, W. W.; Yao, B.; Lia, B. H.; Li, Y. F.; Zheng, J.; Zhang, Z. Z.; Shan, C. X.; Zhang, J. Y.; Shen, D. Z.; Fan, X. W. *Solid State Sci.* **2010**, *12*, 1567−1569.
(15) Tsuji, T.; Terai, Y.; Kamarudin, M. H. B.; Yoshida, K.; Fujiwara, Y. *J. Lumin.* **2012**, *132*, 3125−3128.
(16) Tana, Y.; Fang, Z.; Chen, W.; He, P. *J. Alloys Compd.* **2011**, *509*, 6321−6324.
(17) Khomyak, V. V.; Slyotov, M. M.; Shtepliuk, I. I.; Lashkarev, G. V.; Slyotov, O. M.; Marianchuk, P. D.; Kosolovskiy, V. V. *J. Phys. Chem. Solids* **2013**, *74*, 291−297.
(18) Lupan, O.; Pauporté, T.; Chow, L.; Viana, B.; Pellé, F.; Ono, L. K.; Cuenya, B. R.; Heinrich, H. *Appl. Surf. Sci.* **2010**, *256*, 1895−1907.
(19) Dai, L. L.; Huang, F. Y.; Xiong, D. P.; Tang, X. G.; Chen, J. *Mater. Sci. Forum* **2011**, *687*, 667−672.
(20) Yang, J.; Li, X.; Lang, J.; Yang, L.; Wei, M.; Gao, M.; Liu, X.; Zhai, H.; Wang, R.; Liu, Y.; Cao, J. *Mater. Sci. Semicond. Process.* **2011**, *14*, 247−252.
(21) Armelao, L.; Bottaro, G.; Pascolini, M.; Sessolo, M.; Tondello, E.; Bettinelli, M.; Speghini, A. *J. Phys. Chem. C* **2008**, *112*, 4049−4054.
(22) Fazio, E.; Patanè, S.; Scibilia, S.; Mezzasalma, A. M.; Mondio, G.; Neri, F.; Trusso, S. *Curr. Appl. Phys.* **2013**, *13*, 710−716.
(23) Kumar, V.; Swart, H. C.; Ntwaeaborwa, O. M.; Kroon, R. E.; Terblans, J. J.; Shaat, S. K. K.; Yousif, A.; Duvenhage, M. *Mater. Lett.* **2013**, *101*, 57−60.
(24) Al-Gaashani, R.; Radiman, S.; Daud, A. R.; Tabet, N.; Al-Douri, Y. *Ceram. Int.* **2013**, *39*, 2283−2292.
(25) Gupta, S. K.; Mohapatra, M.; Kaity, S.; Natarajan, V.; Godbole, S. V. *J. Lumin.* **2012**, *132*, 1329−1338.
(26) Benz, F.; Guerra, J. A.; Weng, Y.; Weingärtner, R.; Strunk, H. P. *Phys. Status Solidi C* **2013**, *10*, 109−112.
(27) Uitert, L. G. V.; Iida, S. *J. Chem. Phys.* **1962**, *37*, 986−992.
(28) Kamat, P. V.; Patrick, B. *J. Phys. Chem.* **1992**, *96*, 6829−6834.
(29) Tang, J.; Durrant, J. R.; Klug, D. R. *J. Am. Chem. Soc.* **2008**, *130*, 13885−13891.
(30) Tamaki, Y.; Hara, K.; Katoh, R.; Tachiya, M.; Furube, A. *J. Phys. Chem. C* **2009**, *113*, 11741−11746.
(31) Tamaki, Y.; Furube, A.; Katoh, R.; Murai, M.; Hara, K.; Arakawa, H.; Tachiya, M. *C. R. Chim.* **2006**, *9*, 268−274.
(32) Bauer, C.; Boschloo, G.; Mukhtar, E.; Hagfeldt, A. *Chem. Phys. Lett.* **2004**, *387*, 176−181.
(33) Gür, E.; Tüzemen, S.; Meral, K.; Onganer, Y. *Appl. Phys. A: Mater. Sci. Process.* **2009**, *94*, 549−554.
(34) Tam, K. H.; Cheung, C. K.; Leung, Y. H.; Djurišić, A. B.; Ling, C. C.; Beling, C. D.; Fung, S.; Kwok, W. M.; Chan, W. K.; Phillips, D. L.; Ding, L.; Ge, W. K. *J. Phys. Chem. B* **2006**, *110*, 20865−20871.
(35) Studenikin, S. A.; Cocivera, M. *J. Appl. Phys.* **2002**, *91*, 5060−5065.
(36) Ishizumi, A.; Takahashi, Y.; Yamamoto, A.; Kanemitsu, Y. *Mater. Sci. Eng., B* **2008**, *146*, 212−215.
(37) Liu, Y.; Luo, W.; Li, R.; Liu, G.; Antonio, M. R.; Chen, X. *J. Phys. Chem. C* **2008**, *112*, 686−694.
(38) Cheng, B.; Zhang, Z.; Liu, H.; Han, Z.; Xiao, Y.; Lei, S. *J. Mater. Chem.* **2010**, *20*, 7821−7826.
(39) Li, M.; Xing, G.; Xing, G.; Wu, B.; Wu, T.; Zhang, X.; Sum, T. C. *Phys. Rev. B* **2013**, *87*, 115309.
(40) Vidya, R.; Ravindran, P.; Fjellvåg, H.; Svensson, B. G.; Monakhov, E.; Ganchenkova, M.; Nieminen, R. M. *Phys. Rev. B* **2011**, *83*, 045206.
(41) Patterson, C. H. *Phys. Rev. B* **2006**, *74*, 144432.
(42) Gallino, F.; Pacchioni, G.; Di Valentin, C. *J. Chem. Phys.* **2010**, *133*, 144512-10.
(43) Hu, J.; Pan, B. C. *J. Chem. Phys.* **2008**, *129*, 154706-8.
(44) Lany, S.; Zunger, A. *Phys. Rev. B* **2005**, *72*, 035215.
(45) Kohan, A. F.; Ceder, G.; Morgan, D.; Van de Walle, C. G. *Phys. Rev. B* **2000**, *61*, 15019−15027.
(46) Anderson, J.; Chris, G. V. d. W. *Rep. Prog. Phys.* **2009**, *72*, 126501.
(47) Xing, G. Z.; Lu, Y. H.; Tian, Y. F.; Yi, J. B.; Lim, C. C.; Li, Y. F.; Li, G. P.; Wang, D. D.; Yao, B.; Ding, J.; Feng, Y. P.; Wu, T. *AIP Adv.* **2011**, *1*, 022152.
(48) Teklemichael, S. T.; Oo, W. M. H.; McCluskey, M. D.; Walter, E. D.; Hoyt, D. W. *Appl. Phys. Lett.* **2011**, *98*, 232112-3.